PCCP

COMMUNICATION

View Article Online
View Journal | View Issue

Cite this: *Phys. Chem. Chem. Phys.*, 2024, **26**, 21337

Received 4th July 2024,
Accepted 15th July 2024

DOI: 10.1039/d4cp02664k

rsc.li/pccp

Molecular asymmetry and rigidification as strategies to activate and enhance thermally activated delayed fluorescence in deep-blue MR-TADF emitters†

Rangani Wathsala Weerasinghe,[a] John Marques dos Santos,[b] Youhei Chitose,[ac] Tomas Matulaitis,[b] Stuart L. Warriner,[f] Debasish Barman,[a] Chin-Yiu Chan,*[de] Youichi Tsuchiya,*[a] Eli Zysman-Colman*[b] and Chihaya Adachi*[ac]

Two novel deep-blue multi-resonance thermally activated delayed fluorescence (MR-TADF) emitters, 1B-CzCrs and 2B-CzCrs, containing a fused carbazole unit were synthesized. The carbazole contributed to the emergence of TADF in these small molecules. Particularly, organic light-emitting diodes with 1B-CzCrs doped in the mCP host achieve a maximum external quantum efficiency of 12.8% at CIE coordinates of (0.146, 0.062).

Organic thermally activated delayed fluorescence (TADF) materials have been steadily developed over the past decade for organic light-emitting diodes (OLEDs) due to their ability to convert 100% of the electrically generated excitons to photons without using scarce metals, garnering great interest within the display community.[1,2] Typical TADF emitters consist of donor (D) and acceptor (A) moieties connected in a twisted conformation to result in a minimal orbital overlap between the highest occupied and lowest unoccupied molecular orbitals (HOMO and LUMO, respectively). This provides a small energy splitting (ΔE_{ST}) between the lowest singlet (S_1) and triplet (T_1) excited states.[3] However, such a long-range charge transfer (LRCT) character of these D–A TADF materials leads to a broad emission spectrum (full width of half maximum, FWHM, >45 nm) even in compounds where conformational motion is restricted.[4] Broad emission is undesired for colour saturation. In 2016, Hatakeyama *et al.* reported a new class of TADF materials, so-called multi-resonant TADF (MR-TADF) compounds that typically have a narrowband emission (FWHM of <30 nm).[5] These compounds contain electron-rich and electron-poor dopants disposed *meta* or *para* with respect to each other within a polycyclic aromatic compound. Such compounds emit from a short-range charge transfer (SRCT) state associated with a characteristically small ΔE_{ST}.[6,7] MR-TADF materials not only exhibit narrowband emission but also have high photoluminescence (PL) quantum yields (Φ_{PL}) linked to fast radiative decay rate constants.

On the other hand, examples of deep-blue MR-TADF emitters satisfying the industry standard for high-definition displays *i.e.*, the BT.2020 standard are still limited; indeed, the blue devices must emit at Commission Internationale de l'Éclairage (CIE) coordinates of $CIE_{x,y}$ = (0.131, 0.046).[8–10] In the literature, the strategy of fusing aromatic tertiary amines with boron atoms has been widely used to construct deep-blue MR-TADF emitters. This approach has also been modified by replacing the nitrogen atoms with other heteroatoms, and/or by replacing the often used diphenylamine (DPA) moieties with carbazole (Cz) to achieve color and emissivity control.[6,7] Previously, we reported the deep blue emitters **1B-DTACrs** and **2B-DTACrs** (Table S1, ESI†) wherein the devices emit with $CIE_y \leq 0.05$.[11] **1B-DTACrs** showed near unity Φ_{PL} of 99% but was not TADF, while **2B-DTACrs** was TADF, with a fast RISC rate constant ($k_{RISC} \sim 10^5$); however, the Φ_{PL} was lower at 64%. In this study, we replaced the DTA with Cz and designed and synthesized two deep-blue MR-TADF emitters, **1B-CzCrs** and **2B-CzCrs** (Table S1, ESI†). The optoelectronic properties of the two deep-blue MR-TADF emitters were studied in detail, supported by computations. Interestingly, compared to the previously reported DPA-based **1B-DTACrs**, the Cz-containing **1B-CzCrs** is TADF, as is **2B-CzCrs**. **1B-CzCrs** and **2B-CzCrs** emit at λ_{PL} of 446 and 441 nm, with FWHM of 25 and 19 nm in toluene, respectively and the asymmetric **1B-CzCrs** showed better TADF properties.

[a] *Center for Organic Photonics and Electronics Research (OPERA), Kyushu University, Motooka, Nishi, Fukuoka 819-0395, Japan. E-mail: tsuchiya@opera.kyushu-u.ac.jp*
[b] *Organic Semiconductor Centre, EaStCHEM School of Chemistry, University of St Andrews, St Andrews, KY16 9ST, UK. E-mail: eli.zysman-colman@st-andrews.ac.uk*
[c] *Department of Applied Chemistry, Graduate School of Engineering, Center for Molecular Systems (CMS), Kyushu University, 744 Motooka, Nishi, Fukuoka 819-0395, Japan. E-mail: adachi@cstf.kyushu-u.ac.jp*
[d] *Department of Materials Science and Engineering, City University of Hong Kong, Tat Chee Avenue, Kowloon, Hong Kong, China. E-mail: chinychan2@cityu.edu.hk*
[e] *Department of Chemistry, City University of Hong Kong, Tat Chee Avenue, Kowloon, Hong Kong, China*
[f] *School of Chemistry, University of Leeds, Leeds, LS2 9JT, UK*

† Electronic supplementary information (ESI) available. See DOI: https://doi.org/10.1039/d4cp02664k

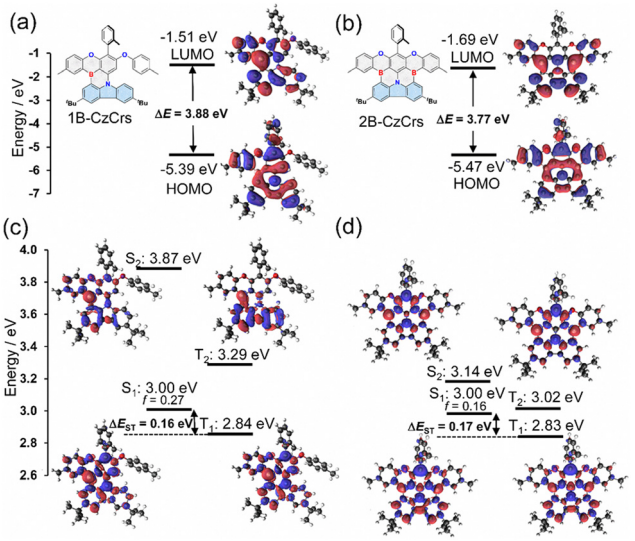

Fig. 1 Theoretical calculation results for **1B-CzCrs** (a) and (c) and **2B-CzCrs** (b) and (d); (a) and (b) HOMO and LUMO distributions at the PBE0/6-31G** level of theory (gas phase), (b) and (d) excited-state difference density plots of S_1, T_1, and T_2 and those energies at the excited-state geometries at the SCS-ADC(2)/cc-pVDZ level of theory. *f* values denote the oscillator strength.

The detailed synthesis procedure, characterization, and electrochemical data of **1B-CzCrs** and **2B-CzCrs** are provided in ESI† (Fig. S1–S19 and Table S2). Thermal gravimetric analysis (TGA) has been carried out for **1B-CzCrs** and **2B-CzCrs** under a nitrogen atmosphere to determine the decomposition temperature (T_d). The T_d values of both emitters were found to be higher than 400 °C, suggesting their high thermal stability (Fig. S20, ESI†).

The ground-state and excited-state geometries of **1B-CzCrs** and **2B-CzCrs** were calculated using Density Functional Theory (DFT) and the post Hartree–Fock methods, respectively. The HOMO–LUMO energy gaps for **1B-CzCrs** and **2B-CzCrs** were calculated as 3.88 eV and 3.77 eV, respectively (Fig. 1). These values are smaller than those reported for **1B-DTACrs** and **2B-DTACrs** (4.03 and 3.91 eV) due to the increased conjugation that results from the incorporation of the fused carbazole moiety (Table S3, ESI†). This trend supports the experimentally obtained values, which are 3.13 and 3.10 eV for **1B-CzCrs** and **2B-CzCrs**, respectively, and 3.17 and 3.05 eV for **1B-DTACrs** and **2B-DTACrs**, respectively (Table S2, ESI†), especially for the monoborylated counterparts. The oscillator strength (f) of the S_0–S_1 transition of **1B-CzCrs** is larger (0.27) than that of **2B-CzCrs** (0.16), while the ΔE_{ST} are essentially the same (0.16 and 0.17 eV) (Table S4, ESI†). The HOMO–LUMO transition in **1B-CzCrs** is purely SRCT, while in **2B-CzCrs** it exhibits more of LRCT character, which is reflected in the lower *f* in the latter. Analysis of the excited-state difference density plots confirmed that the SRCT S_1 state in **1B-CzCrs** is extended over more of the compound compared to **2B-CzCrs**. The nature of the T_1 state in both molecules is essentially the same as the respective S_1 states, yielding comparable ΔE_{ST} in both molecules. More notably, there are significant differences in the nature of the T_2 state, with T_2 of **1B-CzCrs** having more of a LE character on the Cz moiety, while that of **2B-CzCrs** still retains SRCT character, similar to that of S_1 state. This results in a considerably higher spin–orbit coupling (SOC) value in **1B-CzCrs** compared to that in **2B-CzCrs** (Fig. 1).

Fig. 2 shows the absorption and emission spectra of **1B-CzCrs** and **2B-CzCrs** in toluene (1.0×10^{-5} mol dm^{-3}). There are two strong absorption bands, one below 350 nm and the other at around 400 nm that can be attributed to π–π* locally-excited (LE) and SRCT transitions, respectively. The structured absorption bands at 405 and 431 nm of **2B-CzCrs** can be attributed to S_0–S_2 and S_0–S_1 transition, respectively (Fig. 1a). As predicted by the calculated *f* values, there is a stronger S_0–S_1 absorption in **1B-CzCrs** than in **2B-CzCrs**. **1B-CzCrs** and **2B-CzCrs** emit narrowly in the deep-blue region with λ_{PL} of 446 and 441 nm (FWHM of 24 and 19 nm), respectively (Table 1). The corresponding CIE_y were <0.04, indicating a high potential for realizing deep blue OLEDs having high colour purity. Because the MR-TADF core has been rigidified by introducing the Cz moiety, the emissions of **1B-CzCrs** and **2B-CzCrs** are narrower than those of **1B-DTACrs** and **2B-DTACrs** (27 and 21 nm).[11] The ΔE_{ST} was estimated from the difference in the onsets of the fluorescence and phosphorescence spectra after applying the Jacobian conversion at 0.21 and 0.24 eV for **1B-CzCrs** and **2B-CzCrs**, respectively (Fig. S21, ESI†).[12] These values agree well with the theoretical ones calculated at the SCS-ADC(2)/cc-pVDZ level of theory (0.16 and 0.17 eV, respectively).[13] The Φ_{PL} values of **1B-CzCrs** and **2B-CzCrs** in the air are 63 and 55%, respectively, and these significantly increased to 96 and 94% under N_2. This indicates the large contribution of triplets to their light-emitting process. The high Φ_{PL} values can be attributed to their highly rigid structure, resulting in reduced nonradiative decay. However, only a short decay lifetime component was observed in the transient PL for both **1B-CzCrs** and **2B-CzCrs** in toluene (Fig. S22 and S23, ESI†). This is because, despite the high Φ_{PL}, non-radiative decay competes with RISC. The lifetime slightly increases under N_2, indicating that oxygen may affect the singlet radiative decay rates.[14]

On the other hand, a clear delayed decay was observed for both **1B-CzCrs** and **2B-CzCrs** in a 3,3′-di(9*H*-carbazol-9-yl)-1,1′-biphenyl (**mCBP**) host at 5 wt% doping concentration (Fig. 3). It is worth noting that **1B-DTACrs** exhibited no TADF behavior, while **1B-CzCrs** showed delayed emission in host matrices.

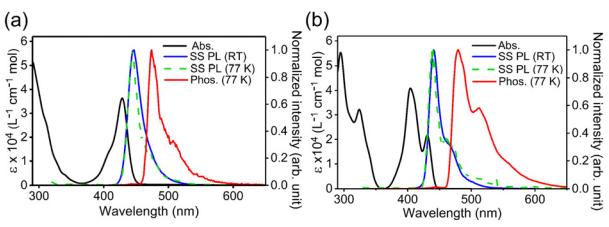

Fig. 2 Absorption (black line), Steady-state (SS) PL at room temperature (RT, blue line), and at 77 K (green dashed line), and phosphorescence (Phos.) at 77 K (red line, delay: 115 ms, gate: 150 ms) for (a) **1B-CzCrs** and **2B-CzCrs** (b) in toluene. λ_{exc} = 310 nm.

Table 1 Photophysical data of **1B-CzCrs** and **2B-CzCrs** in toluene and **mCBP**

	In toluene								5 wt% in **mCBP**								
	Φ_{PL}[a] (%)	τ_p[b] (ns)	λ_{PL} (nm)	FWHM (nm)	S_1[c] (eV)	T_1[d] (eV)	ΔE_{ST} (eV)	$CIE_{x,y}$	Φ_{PL}[a] (%)	τ_p (ns)	τ_d (ms)	λ_{PL} (nm)	FWHM (nm)	k_r[e] (10^7 s^{-1})	k_{nr}[e] (10^7 s^{-1})	k_{ISC}[e] (10^7 s^{-1})	k_{RISC}[e] (10^3 s^{-1})
1B-CzCrs	96 (63)	6.57(5.37)	446	24	2.89	2.68	0.21	0.150, 0.037	67	5.08	0.33	451	28	11.90	5.86	1.88	3.36
2B-CzCrs	94 (55)	8.70(6.52)	441	19	2.91	2.67	0.24	0.142, 0.032	59	8.63	2.98	449	28	5.80	4.03	1.75	0.41

[a] Φ_{PL} were measured using an integrating sphere at λ_{exc} = 310 nm under N_2-saturated and aerated (in parentheses) conditions. [b] τ_p was measured with a streak camera under N_2-saturated and aerated (in parentheses) conditions at λ_{exc} = 355 nm. [c] Estimated from the onset wavelength of the steady-state PL spectrum at 77 K. [d] Estimated from the onset wavelength of the delayed emission spectrum (115–150 ms) at 77 K (λ_{exc} = 310 nm). [e] Rate constants were calculated using the reported method in the literature[15] under the approximation of no phosphorescence contributed to the delayed emission.

The S_1 and T_1 levels of the 5 wt% doped film in **mCBP** are the same as those in toluene, but the PL spectra in **mCBP** are slightly broader, with FWHM of 28 nm for each (Table S5, ESI†). The Φ_{PL} under Ar of 67 and 59% are lower than those in toluene. This behavior was also observed in **1B-DTACrs** and **2B-DTACrs**, but the degree of spectral broadening and the Φ_{PL} drop in **1B-CzCrs** and **2B-CzCrs** are more pronounced. These data suggest that these planar Cz-containing emitters more easily form either aggregates and/or intermolecular interactions with the host in their film state, despite the introduction of *tert*-butyl groups in the skeleton of these compounds in addition to the bulky *o*-tolyl group. This was also confirmed by the narrowing of the emission spectra and the higher Φ_{PL} at lower doping concentrations (Fig. S24, S25, and Table S6, ESI†).

Notably, the delayed emission lifetimes of **1B-CzCrs** and **2B-CzCrs** (0.33 and 2.98 ms, respectively) were significantly longer than that of the **2B-DTACrs** (13.1 μs).[11] The estimated rate constants of radiative and nonradiative decays from S_1 (k_r, and k_{nr}, respectively), intersystem crossing (k_{ISC}), and k_{RISC} are summarized in Table 1.[15] The k_{RISC} values for **1B-CzCrs** and **2B-CzCrs** are 3.36 and 0.41 × 10^3 s^{-1}, respectively; these are a two order difference with that of **2B-DTACrs** (1.3 × 10^5 s^{-1}). There is also a one-order difference in k_{RISC} between **1B-CzCrs** and **2B-CzCrs**. To help explain this difference, SOC magnitude was investigated with PBE0/6-31g(d,p) level of theory in the gas phase (Table S7, ESI†). The SOC value between T_1 and S_1 for **1B-CzCrs** is 0.1187 cm^{-1}, a two-fold higher value compared with that of **2B-CzCrs** (0.0592 cm^{-1}). The SOC values between S_1 and T_2 also reflect this same trend at 0.0995 cm^{-1} and 0.060 cm^{-1} for **1B-CzCrs** and **2B-CzCrs**, respectively. This in itself explains the faster k_{RISC} in **1B-CzCrs** compared with **2B-CzCrs**. Further, considering the energy splitting between S_1–T_1 and S_1–T_2 (0.33 and 0.12 eV for **1B-CzCrs**, 0.40 and 0.08 eV for **2B-CzCrs**, respectively), it is obvious why the asymmetric **1B-CzCrs** has a faster k_{RISC} than the symmetric **2B-CzCrs**. From these results, the replacement of the DPA by Cz in this emitter design has both pros and cons, *i.e.*, turning on TADF yet slowing k_{RISC}. It is however noteworthy that the asymmetry in **1B-CzCrs** leads to faster k_{RISC} than in **2B-CzCrs** while this was not the case with the **1B-DTACrs**/**2B-DTACrs** family.

Temperature-dependent transient emission decay profiles for 5 wt% doped films of **1B-CzCrs** and **2B-CzCrs** under vacuum demonstrate that the delayed emission components of both emitters are thermally activated yet become shorter with increasing temperature (Fig. S26, ESI†). The activation energy for the ISC (E_a^{ISC}) and RISC (E_a^{RISC}) processes and the effective SOCME was estimated from the intercept (Fig. S27 and Table S8, ESI†).[10] The experimentally estimated ΔE_{ST}, that is $E_a^{RISC} - E_a^{ISC}$, was larger for **1B-CzCrs** (65.9 meV) than for **2B-CzCrs** (19.9 meV). However, the significantly larger effective SOC strength of **1B-CzCrs** (0.0181 and 0.0173 cm^{-1} for k_{nr}^S = 0 and k_{nr}^T = 0, respectively) compared to **2B-CzCrs** (0.0029 and 0.0027 cm^{-1} for k_{nr}^S = 0 and k_{nr}^T = 0, respectively) explains the overall enhanced TADF in the former compared to the latter. This provides clear evidence of the contribution of the T_2 state to the RISC process of **1B-CzCrs**.

We also investigated the film state photophysics of **1B-CzCrs** and **2B-CzCrs** in a 1,3-di(9*H*-carbazol-9-yl)benzene (**mCP**) host matrix. Unlike in **mCBP**, both emitters exhibited slightly broadened and red-shifted emission in **mCP**, even at 1 wt% doping concentrations (Fig. S28, S29, and Table S9, ESI†). This can be ascribed to the more polar nature of **mCP**, which has a higher dipole moment (1.35 D), compared to **mCBP** (0.8 D).[16,17] Nonetheless, suppressed aggregation formation was observed upon increasing the doping concentration for both emitters in **mCP** compared to the emitters

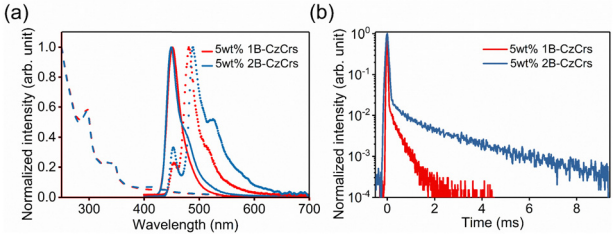

Fig. 3 Photophysical properties of 5 wt% **1B-CzCrs** and **2B-CzCrs** doped in **mCBP**; (a) normalized absorption (dashed lines), SS PL at RT (solid lines, λ_{exc} = 310 nm), and phosphorescence at 77 K (dotted lines, λ_{exc} = 310 nm), (b) transient PL decays (λ_{exc} = 355 nm) at RT.

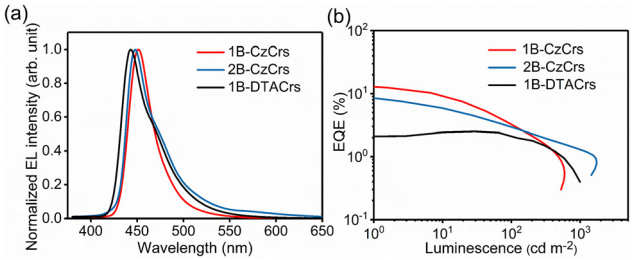

Fig. 4 Device performance with 5 wt% **1B-CzCrs** and **2B-CzCrs** in **mCP**; (a) EL spectra at 100 cd m^{-2}, and (b) EQE-L profile.

Table 2 Device performance of 5 wt% **1B-CzCrs** and **2B-CzCrs** in **mCP**

	V_{on}[a] (V)	EQE_{max}[b] (%)	$EQE_{100/500}$ (%)	λ_{EL} (nm)	$CIE_{x,y}$
1B-CzCrs	3.8	12.8	3.3/0.9	451	0.146, 0.062
2B-CzCrs	3.7	8.4	2.9/1.7	450	0.153, 0.143

[a] Turn-on voltages were estimated as 1 cd m^{-2}. [b] Maximum external quantum efficiencies were estimated at 1 cd m^{-2}.

in **mCBP** (Fig. S24 and S28, ESI†). Stabilizing the excited states of individual MR-TADF dopant molecule within the **mCP** host matrix by relatively stronger dipole–dipole interactions and limiting their aggregation can explain this observation. However, a reduction in Φ_{PL} was observed for the 1 wt% doped film of **1B-CzCrs** in both hosts, due to an insufficient energy transfer between the hosts and the emitter (Fig. S30, ESI†).

To investigate the electroluminescence (EL) properties of **1B-CzCrs** and **2B-CzCrs**, TADF-OLEDs were fabricated by vacuum deposition; the OLED with **1B-DTACrs** was also fabricated as a reference. The following device structure using **mCP** as the host provided the best maximum external quantum efficiency (EQE_{max}): indium-tin-oxide (**ITO**, 100 nm)/**HAT-CN** (10 nm)/**TAPC** (30 nm)/**mCP** (10 nm)/**mCP:** 5 wt% of **1B-CzCrs**, **2B-CzCrs** or **1B-DTACrs** (20 nm)/**PPT** (10 nm)/**TmPyPB** (30 nm)/**Liq** (2 nm)/**Al** (100 nm). All the device data are depicted in Fig. 4 and Fig. S31, S32 (ESI†), Table 2 and Table S10 (ESI†). The OLED with **1B-CzCrs** exhibited a higher EQE_{max} of 12.8% than the device with **2B-CzCrs** (EQE_{max} of 8.4%). The EL of **1B-CzCrs** and **2B-CzCrs** was observed at λ_{EL} of 451 and 450 nm, similar to the corresponding PL emission in **mCP**. Both devices demonstrated a relatively low turn-on voltage below 4.0 V. Furthermore, the device with **1B-CzCrs** showed a much higher EQE_{max} of 12.8% than that with **1B-DTACrs** (2.1%). This, again, confirms that TADF is operational in the former and not the latter. To investigate the molecular orientation of both emitters, angle-dependent PL measurements were performed on the 5 wt% doped emitters in **mCP** films (Fig. S33, ESI†). Given that the horizontal-dipole ratios (Θ) values of 0, 0.33, and 1 correspond to the perfectly horizontal, isotropic, and vertical orientations, respectively, the obtained Θ values for **1B-CzCrs** (0.43) and **2B-CzCrs** (0.50) indicate that the transition dipole moment of both emitters adopts a slightly vertical orientation in **mCP**, reducing the light-outcoupling efficiencies of both emitters below 20% (Table S11, ESI†). The theoretical EQE values estimated for the devices with **1B-CzCrs** and **2B-CzCrs** were 13.3 and 9.5%, respectively, and were in agreement with the experimental data.

The PL emissions of 1 wt% doped film of **1B-CzCrs** and **2B-CzCrs** in **mCBP** host have CIE coordinates closer to the BT.2020 standard for blue (Table S6, ESI†). Although the OLEDs with 1 wt% doped **1B-CzCrs** and **2B-CzCrs** in mCBP host gave $CIE_y < 0.05$, the EQE_{max} values were inferior compared to the devices using **mCP** as the host (Fig. S34 and Table S12, ESI†). This can be ascribed to a charge carrier imbalance that is reflected in the higher turn-on voltage of these devices compared to those using **mCP** as the host.

In conclusion, two deep-blue emitters, **1B-CzCrs** and **2B-CzCrs**, were developed to assess the impact of incorporating a Cz moiety within this small MR-TADF core. The Cz moiety contributed to turning on TADF in both emitters, but slowed the k_{RISC}, especially in the case of the symmetric **2B-CzCrs**. Nonetheless, we present here a comparative example that shows superior photophysical and device performance for the asymmetric design of **1B-CzCrs**, which we believe is a promising strategy that can be applied in future designs of MR-TADF emitters. Despite the introduction of several large steric hindrance units, these two emitters were prone to aggregate. The poorer device efficiencies in **mCP** could be rationalized due to the slightly vertical dipole orientation of the emitters in this host. Nonetheless, the device with **1B-CzCrs** in **mCP** could almost realize the BT.2020 for blue with CIE of (0.146, 0.06) along with a moderate EQE of 12.8%, a significant improvement over the device with **1B-DTACrs**.

The authors acknowledge Ms N. Nakamura and Ms K. Kusuhara for their technical assistance. This work was supported financially by Kyulux Inc, JSPS Grant-in-Aid for Specially Promoted Research (23H05406), JST CREST (JPMJCR22B3), JSPS KAKENHI (23K20039), ESPRC (EP/R035164/1, EP/W007517/1), City University of Hong Kong (Project No. 9610637 and 9231531).

Data availability

This research data supporting this publication can be accessed at **https://doi.org/10.17630/2fd8e197-e110-4fe2-ba94-2471629aaa09**.

Conflicts of interest

There are no conflicts to declare.

References

1 H. Uoyama, K. Goushi, K. Shizu, H. Nomura and C. Adachi, *Nature*, 2012, **492**, 234–238.
2 M. Y. Wong and E. Zysman-Colman, *Adv. Mater.*, 2017, **29**, 1605444.
3 A. Endo, K. Sato, K. Yoshimura, T. Kai, A. Kawada, H. Miyazaki and C. Adachi, *Appl. Phys. Lett.*, 2011, **98**, 083302.
4 Y. J. Cho, S. K. Jeon, S.-S. Lee, E. Yu and J. Y. Lee, *Chem. Mater.*, 2016, **28**, 5400–5405.
5 T. Hatakeyama, K. Shiren, K. Nakajima, S. Nomura, S. Nakatsuka, K. Kinoshita, J. Ni, Y. Ono and T. Ikuta, *Adv. Mater.*, 2016, **28**, 2777–2781.
6 H. J. Kim and T. Yasuda, *Adv. Opt. Mater.*, 2022, **16**, 2201714.
7 M. Mamada, M. Hayakawa, J. Ochi and T. Hatakeyama, *Chem. Soc. Rev.*, 2024, **53**, 1624–1692.
8 R. W. Weerasinghe, S. Madayanad Suresh, D. Hall, T. Matulaitis, A. M. Z. Slawin, S. Warriner, Y. Lee, C. Chan, Y. Tsuchiya, E. Zysman-Colman and C. Adachi, *Adv. Mater.*, 2024, **36**, 2402289.
9 J. Ochi, Y. Yamasaki, K. Tanaka, Y. Kondo, K. Isayama, S. Oda, M. Kondo and T. Hatakeyama, *Nat. Commun.*, 2024, **15**, 2361.
10 J. Bae, M. Sakai, Y. Tsuchiya, N. Ando, X.-K. Chen, T. B. Nguyen, C.-Y. Chan, Y.-T. Lee, M. Auffray,

H. Nakanotani, S. Yamaguchi and C. Adachi, *Front. Chem.*, 2022, **10**, 990918.

11 C.-Y. Chan, S. Madayanad Suresh, Y.-T. Lee, Y. Tsuchiya, T. Matulaitis, D. Hall, A. M. Z. Slawin, S. Warriner, D. Beljonne, Y. Olivier, C. Adachi and E. Zysman-Colman, *Chem. Commun.*, 2022, **58**, 9377–9380.

12 J. Mooney and P. Kambhampati, *J. Phys. Chem. Lett.*, 2013, **4**, 3316–3318.

13 D. Hall, J. C. Sancho-García, A. Pershin, G. Ricci, D. Beljonne, E. Zysman-Colman and Y. Olivier, *J. Chem. Theory Comput.*, 2022, **18**, 4903–4918.

14 N. Notsuka, H. Nakanotani, H. Noda, K. Goushi and C. Adachi, *J. Phys. Chem. Lett.*, 2020, **11**, 562–566.

15 Y. Tsuchiya, S. Diesing, F. Bencheikh, Y. Wada, P. L. dos Santos, H. Kaji, E. Zysman-Colman, I. D. W. Samuel and C. Adachi, *J. Phys. Chem. A*, 2021, **125**, 8074–8089.

16 F. Rodella, S. Bagnich, E. Duda, T. Meier, J. Kahle, S. Athanasopoulos, A. Köhler and P. Strohriegl, *Front. Chem.*, 2020, **8**, 657.

17 S. Ihn, D. Jeong, E. S. Kwon, S. Kim, Y. S. Chung, M. Sim, J. Chwae, Y. Koishikawa, S. O. Jeon, J. S. Kim, J. Kim, S. Nam, I. Kim, S. Park, D. S. Kim, H. Choi and S. Kim, *Adv. Sci.*, 2022, **9**, 2102141.